

# Radio Observations of the 13hr *XMM/ROSAT* Deep X-ray Survey Area

N. Seymour,<sup>1,2,\*</sup> I.M. McHardy<sup>2</sup> & K.F. Gunn<sup>2</sup>

<sup>1</sup>*Institut d'Astrophysique de Paris, 98bis. Boulevard Arago, 75014 Paris, France*

<sup>2</sup>*Department of Physics and Astronomy, University of Southampton, Highfield, Southampton, SO17 1BJ, UK*

DRAFT VERSION

## ABSTRACT

In order to determine the relationship between the faint X-ray and faint radio source populations, and hence to help understand the X-ray and radio emission mechanisms in those faint source populations, we have made a deep 1.4 GHz Very Large Array radio survey of the  $13^h +38^\circ$  *XMM/ROSAT* X-ray Survey Area. From a combined data set of 10hours B configuration data and 14hours A configuration data, maps with  $3.35''$  resolution and a noise limit of  $7.5 \mu\text{Jy}$  were constructed. A complete sample of 449 sources was detected within a  $30'$  diameter region above a  $4\sigma$  detection limit of  $30 \mu\text{Jy}$ , at the map centre, making this one of the deepest radio surveys at this frequency. The differential source count shows a significant upturn at sub-milliJansky flux densities, similar to that seen in other deep surveys at 1.4 GHz (e.g. the Phoenix survey), but larger than that seen in the HDF which may have been selected to be under-dense. This upturn is well modelled by the emergence of a population of medium redshift starforming galaxies which dominate at faint flux densities. The brighter source counts are well modelled by AGNs.

**Key words:** surveys - radio continuum - galaxies: active

## 1 INTRODUCTION

In recent years, deep radio surveys (e.g. Windhorst et al. 1990; Condon 1989; Prandoni et al. 2001; Richards 2000; Hopkins et al. 1998; Bondi et al. 2003; Hopkins et al. 2003; Gruppioni et al. 1999; Ciliegi et al. 1999, etc.) have shown that there is an upturn in the differential radio source counts, normalised to a Euclidean value, below  $\sim 1 \text{ mJy}$ . This upturn has generally been interpreted as the emergence of a new population of starforming galaxies (e.g. Condon 1989; Rowan-Robinson et al. 1993; Garrett et al. 2001) which does not show up at higher flux densities, where number counts are dominated by AGN. Given the strong correlation between 1.4 GHz radio flux and the far infrared flux (Helou et al. 1985; Carilli & Yun 2000), which is itself a starformation rate indicator, radio luminosities can now be used as an independent measure of the starformation rate and, combined with other data, as a way of deconvolving the contribution of AGN and starbursts to the energy budget of the universe.

In order to investigate the nature of the objects that contribute to the X-ray Background radiation (XRB) a deep X-ray survey (McHardy et al. 1998) with *ROSAT* was performed, using the *PSPC* detector, of a field at RA 13 34 37

Dec 37 54 44 (J2000). 96 sources were detected in a  $30'$  diameter field above a flux limit of  $2 \times 10^{-15} \text{ erg cm}^{-2} \text{ s}^{-1}$  in the 0.5 – 2.0 keV band. The majority of the identifications were with broad line AGN, but some galaxies with narrow optical emission lines, known as narrow emission line galaxies (NELGs), were found. These galaxies had a range of X-ray luminosities from  $\sim 10^{40}$  to  $\sim 10^{43} \text{ erg s}^{-1}$ , and a wide range of X-ray/optical ratios and optical emission line ratios. The highest X-ray luminosity yet found for a starburst galaxy is  $\sim 10^{42} \text{ erg s}^{-1}$  (Moran et al. 1999; Halpern et al. 1995) and so the higher luminosity NELGs are most likely to be obscured AGN. However the lower luminosity NELGs, with low ( $\sim 0.01 - 0.001$ ) X-ray/optical ratios could easily be explained by starburst emission (e.g. Gunn et al. 2001). Our conclusion was that the X-ray emission from NELGs, both as a sample and within individual galaxies, is due to a mixture of AGN and starbursts.

As a starburst is associated with radio emission (e.g. Condon 1992) then, if some of the NELG X-ray emission is produced by starbursts, one would expect detectable, associated radio emission; steep radio spectrum emission, detected and resolved on galaxy scales, would be a very strong starburst indicator (e.g. Condon 1992). Preliminary 1.4 GHz observations made with the Very Large Array (VLA) radio telescope of the US National Radio Astronomy Obser-

\* E-mail: seymour@iap.fr

vatory<sup>1</sup> were reported in McHardy et al. (1998). We noted that 4 of the 10 brightest NELGs were detected as radio sources whereas a much lower fraction of X-ray QSOs was detected indicating that complementary radio observations would help determine the emission processes of these NELGs.

In order to improve on the significance of this early result we carried out deeper observations with the VLA at 1.4 GHz, and at 5 GHz, of the 30' diameter X-ray survey area. At 1.4 GHz the primary beam diameter of the VLA is 30' and so the whole X-ray field can be covered in a single pointing. Thus the X-ray and 1.4 GHz radio fields are very well matched. At 5 GHz, due to the smaller size of the primary beam, we have to make a number of pointings, over a grid of positions, in order to fully cover the X-ray field. We also performed higher resolution ( $\sim 0.2''$  beam) observations with MERLIN at 1.4 GHz. The ultimate aim is to resolve and detect any extended radio emission on galaxy scales out to redshifts  $z > 0.5$  and to determine the radio spectra of the various sources.

X-ray spectra are also a strong diagnostic of the emission mechanism, e.g. soft thermal spectra would be associated with starburst emission. With *XMM-Newton*, we therefore made a very deep (200ksec) observation (Page et al. 2003; Loaring et al. 2004, in preparation), providing high quality X-ray spectra in the 0.1–12 keV band, and detecting fainter X-ray sources than are seen in the *ROSAT* survey. In order to provide X-ray positions of sub arcsecond accuracy, and hence unambiguous identifications, we also observed the 13hr field for  $4 \times 30$ ksec with the *Chandra* ACIS-I instrument (McHardy et al. 2003). We detected 214 X-ray sources. A preliminary analysis of the X-ray/radio relationship, based on these new data, is given by Gunn et al. (2003).

In this paper we present the new 1.4 GHz VLA observations. The 5 GHz observations are described in Seymour 2002, and the MERLIN observations and a detailed correlation of the X-ray and radio sources will be presented elsewhere. The observations and data reduction are described in Section 2. We note that our observational set-up and analysis techniques are similar to those of Richards (2000), to whom we refer readers for a more detailed description. The source extraction is described in Section 3. This 1.4 GHz survey is comparable in depth to the deepest surveys previously made at this frequency (e.g. Richards 2000; Hopkins et al. 2003, and references therein) and we detect sources at  $4\sigma$  significance down to  $30 \mu\text{Jy}$  at the map centre. We are therefore able to define accurately the shape of the source counts below 1 mJy. In Section 4 we present these source counts, compare them with previous results and model them. The radio/optical/X-ray cross-correlation will be presented in future papers.

## 2 OBSERVATIONS AND DATA REDUCTION

In November 1995 the 13hr field was observed for 10 hours at 1.4 GHz by the VLA in the B configuration. Observations were made in multi-channel continuum spectral line

mode with two sets of  $8 \times 3.125$  MHz channels to minimise chromatic aberration, centred on intermediate frequencies 1.365 GHz and 1.435 GHz. Each channel was composed of two independent circular polarisations. This observational arrangement is known as ‘4IF’ mode, in VLA parlance. These observations were followed in August 1998 by 3 observations of 10hrs each in the A configuration. These observations were also made in 4IF mode, centred on the same frequencies as before.

### 2.1 Initial Data Reduction

Both the A and B configuration observations were calibrated with the same primary and secondary calibrators, 1331+305 (3C286) and 1310+323, for amplitude and phase respectively. As the observations were made in spectral line mode, bandpass calibrators were also needed, 1310+323 for the A configuration data and 1331+305 for the B configuration data. The B configuration data was calibrated using the standard recipe for spectral line data within the NRAO AIPS software. After removing the sidelobes of bright sources outside the X-ray survey area from the data, the noise level of the B configuration map was close to the theoretical thermal noise level.

Of the 24 hours on-source during the A configuration observations, 10 hours were lost, or unusable, mainly due to thunderstorm related problems which lead to power outages at some of the antennae, correlator problems and high interference. The remaining 14 hours of good data were calibrated and mapped in the standard fashion with AIPS. However heavy cleaning and careful positioning of CLEAN boxes were not sufficient to remove fully the sidelobes of bright sources and thus reach the thermal noise limit. It was therefore necessary to self-calibrate the A configuration data. The B configuration data did not require self calibration.

### 2.2 Self-calibration of the data

The brightest source near the field is an extended source on the western edge of the primary beam. This source is known as J133328.7+375553 in the FIRST radio survey (White et al. 1997) and has a flux density of 92 mJy at 1.4 GHz. Hereafter it is referred to as source 1, in Table A1. It has a linear size of  $\sim 40''$  which is just beyond the limit of extended structure detectable by the VLA in A configuration. It is the brightest source near the field by almost an order of magnitude and its residual sidelobes, after cleaning, were the major noise contributors to maps of the area within the primary beam. The next 3 brightest sources within the primary beam could also not be deconvolved properly, even after many CLEAN iterations. Ripples typical of phase calibration errors were visible in the maps made with the A configuration data.

Traditionally, self-calibration has been restricted to fields containing one or more bright sources near the centre. Obtaining the theoretical dynamic range of wide field data like ours has often been done by imaging the interfering sources to create a model which can then be subtracted from the UV data set, known as uvsubbing. This method was attempted very carefully channel by channel, but the residual sidelobes across the field remained. The reason why this

<sup>1</sup> The National Radio Astronomy Observatory is a facility of the National Science Foundation operated under cooperative agreement by Associated Universities, Inc.

method fails is not entirely clear, but it is likely to be linked to the angular size of source 1. It was easily bright enough for the extended emission to be detected, but the minimum antenna spacings of the VLA A configuration meant that it was difficult to obtain a good enough model to uvsb especially with its location so close to the edge of the primary beam where beam effects change rapidly. Recently self-calibration has been applied successfully to fields containing only relatively faint sources in the centre, such as are common in deep survey work (e.g. Ivison et al. 2002; Smail et al. 2002, and references therein). Our field has a handful of sources of flux density  $\geq 10$  mJy within, or close to the edge of, its primary beam and so is quite satisfactory for self calibration, so here we include all the sources in our field, including source 1.

To obtain an input model on which to self-calibrate the data, we first made  $4 \times 4096$  maps with  $0.22''$  pixels to cover the full X-ray field. We carried out  $10^5$  CLEAN iterations and also included separate CLEAN boxes around 3 bright sources lying not far beyond the edge of the primary beam (see Fig. 1). All of the CLEAN components from the above mapping were used as a model for self calibration. CALIB was run twice, iteratively, in the self-calibration procedure, solving for phase weighted by amplitude each time. After each run of CALIB a new map was made to obtain a new input model. For the first run the solution interval was 60mins and for the second run the interval was 20mins, comparable with the time between observations of the phase calibrator. A  $w$  range of  $20 - 500k\lambda$  was used to emphasise the emission from Fourier components on scales of  $0.4 - 10''$ , where the model best represents the sky brightness. Data outside this range were given a relative weight of 0.1 to reduce the contribution from very small and very large scale structures, which are mostly spurious. This procedure led to 6.9 per cent of the A configuration data being flagged out, but the ripples were almost completely removed. Prior to self-calibration, the rms noise of the image in the best parts of the field was  $\sim 12 \mu\text{Jy}/\text{beam}$ , but was considerably higher near to bright sources. After self-calibration the rms noise level, for the A configuration data, was  $\sim 10 \mu\text{Jy}/\text{beam}$  across almost the whole field, with areas near to bright sources showing the greatest improvement.

### 2.3 The Image Construction

The A and B configuration data were then combined using the AIPS algorithm DBCON. The relative weighting of the data sets was determined from the ‘sum of the gridding weights’ reported by the AIPS task IMAGR, leading to the DBCON parameter REWEIGHT = 1, 0.868445. A multifaceted imaging strategy was used so that no part of the survey field was too far from the centre of an individual facet image. To produce accurate positions, we covered the  $30'$  field of view with a square array of  $9 \times 2048$  pixel maps, with  $0.33''/\text{pixel}$ . This pixel scale adequately samples the A configuration restoring beam of  $1.4''$ . This mapping strategy was used to correct for the fact that we are approximating the curvature of the celestial sphere to a plane. Due to the computing power available it was possible to deconvolve each field simultaneously in IMAGR and use the DO3D option (available in more recent versions of AIPS) which reprojects the coordinates of the Fourier transform plane to the centre of each facet. The maps were shifted about  $100''$

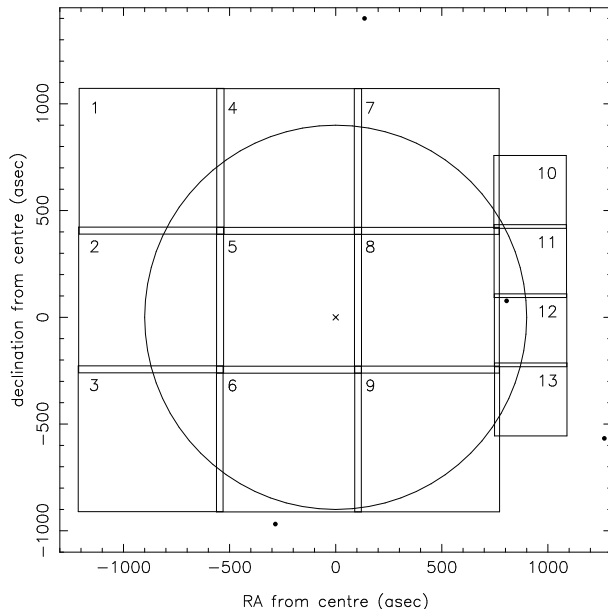


**Figure 1.** A figure to show the mapping strategy. Maps 1 to 9 are  $2048 \times 2048$  pixels and maps 10 to 13 are  $1024 \times 1024$ . The scale is  $0.33''/\text{pixel}$ . The cross in map 5 indicates the centre of the XMM-Newton and ROSAT field of view, and the VLA phase pointing centre. The small filled circle in map 12 indicates the location of the brightest source in the region, known as source 1 in Table A1. The locations of three other confusing sources are also indicated by small filled circles.

west to avoid source 1, which had caused problems in the calibration. The slice of the circular field of view that was missed was imaged separately with four  $1024 \times 1024$  maps in a vertical stripe (see Fig. 1).

The final maps were made using natural weighting of the  $wv$  data, to obtain the most sensitive maps, which gave a restoring beam for the combined data of  $3.35''$ . The final set of 13 maps (Fig. 1) were constructed with  $10^6$  CLEAN iterations and a GAIN value of 0.1. All fields, except the flanking field containing source 1 and the flanking field immediately above it, had pixel noise that was well fitted by a Gaussian distribution with an average rms of  $7.5 \mu\text{Jy}/\text{beam}$ , prior to correction of attenuation by the primary beam. Source detection (see Section 3.1) was performed on the array of maps described above, but for display purposes only, we have produced a  $4096 \times 4096$  pixel map, with pixel size  $0.33''$ , covering the inner  $22.8'$  by  $22.8'$  of the field (Fig. 2). This map was produced with a less detailed cleaning strategy and has an rms noise of  $10 \mu\text{Jy}/\text{beam}$ .

## 3 THE COMPLETE SOURCE CATALOGUE

### 3.1 Source Extraction

The AIPS algorithm SAD (Search And Destroy) was used to detect small, and unresolved sources in the maps by fitting two-dimensional elliptical Gaussians. This task is poor at determining the flux density of extended sources as it tries to split them up into small Gaussians. The flux densities of extended sources were therefore determined by hand using the AIPS algorithm TVSTAT which finds the total flux density

This figure is available in the full version of the paper at [www.2.iap.fr/users/seymour/](http://www.2.iap.fr/users/seymour/)

**Figure 2.** An inverse greyscale image of the inner 22.8' by 22.8' of the 1.4 GHz map. This map has a pixel size of 0.33'', is 4096 pixels square and was made with an effective resolution of 3.35'', for display purposes only. Note that this image has not been corrected for primary beam attenuation.

in an irregular area defined by the user. However there were only 7 sources, with peak flux density above our detection threshold, where SAD failed due to extended morphology. SAD was initially instructed to search for sources above a three sigma peak flux density (ie 22.5  $\mu$ Jy), below the final robust detection limit of 30  $\mu$ Jy ( $4\sigma$ ). This was done to ensure SAD extracted all sources close to the  $4\sigma$  detection limit where SAD was found to be not so efficient. The search was performed on maps prior to correction of the primary beam attenuation. Therefore, after correction, the  $3\sigma$  detection limit would be 22.5  $\mu$ Jy at the phase centre, but 45  $\mu$ Jy at the edge of the X-ray field, i.e. 15' from the centre. Each source above  $4\sigma$  was checked visually to see if it was spurious (e.g. part of a residual side-lobe) and 12 were discarded for this reason. Additionally all the residual maps produced by SAD were inspected for possible real sources with a peak flux density  $> 4\sigma$  which had been missed by SAD. This was done by producing contoured maps of the field with the lowest contour at  $4\sigma$ . This led to only 3 more sources being included, all in the 4 – 5 $\sigma$  range, all in areas of above average noise. Although slightly subjective this method did not change the final catalogue significantly. Finally all sources with peak flux density  $< 4\sigma$  were removed from the catalogue.

### 3.1.1 The 6'' Resolution Map

In order to look for low surface brightness objects in the field a map was constructed in exactly the same fashion as before except that it was tapered to have a resolution of  $\sim 6''$ , thereby increasing the sensitivity to low surface brightness sources. The tapered image had an rms of 12.5  $\mu$ Jy and a natural restoring beam of 6.07''. The sources were extracted with SAD, verified in the same manner as before and the list correlated with the original catalogue to look for new sources. Four new, slightly extended sources with a peak flux density above  $4\sigma$  in the tapered map (ie  $> 50 \mu$ Jy) were discovered and added to the final catalogue which is listed in table A1.

## 3.2 Flux Density Correction Factors

Here we briefly discuss the main factors which distort the true flux density of sources. For more details see Richards (2000).

### 3.2.1 SAD Bias

There is a known bias in the SAD elliptical fitting algorithm (Condon 1997) which at low signal/noise overestimates a source's angular size due to fluctuations in the noise at the edge of a source. As the total flux density is calculated from the total angular size and the peak flux density, which is not affected by this bias, the total flux density is overestimated. This effect was investigated by making 3 separate

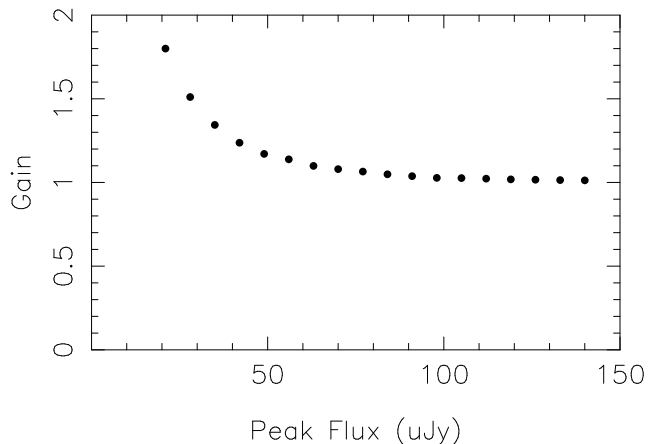


**Figure 3.** A plot of the average measured fractional increase in total flux density for model point sources inserted into the residual data and then detected by SAD, as a function of the input peak flux density.

simulations where, in each simulation, 64 fake sources of a given flux density were inserted into each of the nine residual images left after the running of SAD (i.e. the original maps with all the sources found by SAD removed). These fake sources were inserted with the task IMMOD and then extracted by SAD, having been visually inspected to check that no sources were coincident with any artifacts in the residual maps caused by the initial execution of SAD. This procedure was repeated for fake sources with peak flux density between 140  $\mu$ Jy and 21  $\mu$ Jy, at intervals of 7  $\mu$ Jy. It was then possible to plot the average overestimate of the total flux density of a source as a function of peak flux density.

Figure 3 shows how the fractional overestimate increases with decreasing flux density. An empirical polynomial curve was fitted to the relationship and was then used to correct the total flux density of every source. From the simulations it was also possible to calculate the fraction of sources that are undetected by SAD as a function of peak flux density (see Figure 4). This relationship was also fitted with an empirical polynomial curve and is later used for calculating the completeness of the differential source counts (Section 4).

### 3.2.2 Instrumental Corrections

There are four instrumental corrections which need to be considered; Primary Beam Attenuation, Chromatic Aberration (Bandwidth Smearing), Time Delay Smearing and 3D Smearing. These corrections are discussed below.

#### (i) Primary Beam Attenuation

The ultimate limiting factor to the field of view is the beam pattern of the individual antennae. For the VLA at 1.4 GHz the full width at half power of the beam pattern is  $\sim 30'$ . The empirically measured primary beam attenuation

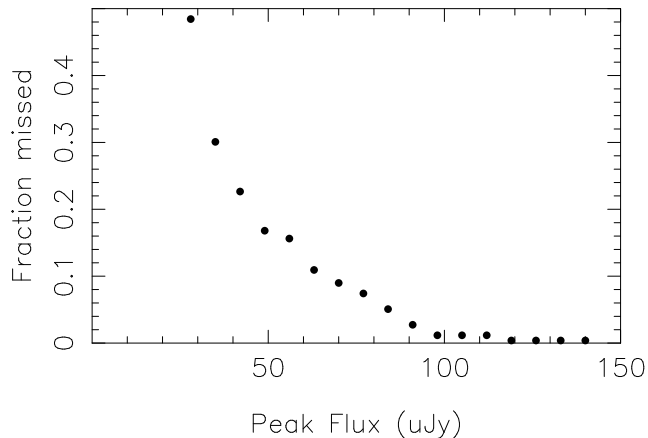


**Figure 4.** A plot of the average fraction of sources inserted into the residual data which are not detected by SAD shown as a function of the input peak flux density.

as a function of distance from the pointing centre, as given in the explain file for the AIPS task PBCOR, was used to correct the measured peak and integrated flux densities of the sources, although the signal to noise given in Table A1 is the empirically measured one which is not affected by the primary beam attenuation.

(ii) Chromatic Aberration

Chromatic aberration, also known as bandwidth smearing, leads to sources far from the phase centre being smeared in a radial direction, with the smearing being greater for larger observing bandwidths. The peak flux density is less than would be measured with an infinitesimally narrow observing band, but the total flux density is conserved. Although the current ‘4IF’ observing set up was selected to minimise the effects of chromatic aberration, whilst not sacrificing sensitivity, it is still a small consideration for sources far from the field centre. Richards (2000) has determined empirically a relationship, for point sources, between the observed peak flux density and the true peak flux density (= the integrated flux density, for point sources) for the same ‘4IF’ observing set up that we used. The relationship is

$$\frac{S_{\text{peak flux}}}{S_{\text{integrated flux}}} = \left\{ 1 + \left( \frac{r}{k} \right)^2 \right\}^{-0.5} \quad (1)$$

where  $r$  is the distance from the field centre in arcminutes and  $k$  was found to be 16.19’ from a least squares fit to the off-axis measurements of the peak and integrated flux density of the calibrator source 1400+621. We have used this formula to correct the peak flux densities of unresolved sources. This formula was also used to estimate the fraction of sources missed in each bin of the differential source counts due to the decrease in sensitivity to peak flux densities away from the centre.

(iii) Time Delay Smearing

During observations the antennae continuously move through the UV plane, sampling different parts of the Fourier transform of the sky brightness. Long integrations therefore lead to averaging of the signal and consequent distortion of the image. To minimise this ‘time delay smearing’ we used the minimum 3.3 second sampling interval in

all observations. Using the relationship given in Chapter 18 of Synthesis Imaging II (Taylor et al. 1999) at the furthest distance from the phase centre we will have a maximum reduction in the peak flux densities of  $< 0.1\%$  which we did not correct for.

(iv) 3D smearing

A source may be smeared during imaging when the sky is approximated to a flat plane. Our mapping strategy to address is discussed in section 2.3. To test the positional accuracy of each source the positions of sources measured from maps made with large fields of view (e.g. Fig. 2) were compared with those from small 30’’ ‘postage-stamp’ maps. It was found that the discrepancies in position were all better than 0.3’’ with no systematic offsets as a function of distance from either the pointing centre or the map centres.

Additionally, the positions of non-extended sources were also compared with those of potential  $R$ -band optical counterparts (M’Hardy et al. 2003) within 1’’ of the radio source position. Again no systematic offsets were found. Our paper on the radio/optical correlation (in preparation) will explain the matching of optical counterparts in more detail. No corrections for the annual aberration effect were made which leads to an discrepancy of almost an order of magnitude less than the error due to 3D smearing. Total positional errors are discussed more in Section 3.3.

### 3.3 Catalogue construction

#### 3.3.1 Double Sources

In previous radio surveys a variety of different criteria have been used to determine whether two nearby unresolved sources are actually components of one double source, e.g. a flux ratio  $\leq 2$  and separation  $\leq 2 \times$  the restoring beam (Ciliegi et al. 1999). Prandoni et al. (2000) compared the nearest neighbour density pair distribution function of their catalogue against one expected for a random distribution of sources in the sky. They then derived the angular distance required to discriminate between real and unreal physical associations. None of the sources in our catalogue could be considered to be components of a double under the criteria of Ciliegi et al. (1999). If this criteria were relaxed to a flux ratio  $\leq 3$  and a separation  $\leq 3 \times$  the restoring beam we obtain 11 pairs. From visual inspection only the two brightest pairs appear to be real associations. The first is a single slightly extended source associated with a spiral galaxy which SAD has mistakenly resolved into two components. The second appears to be two lobes of the same source with an optical counterpart between them which we use to give the position of the radio source. It is possible that there may be further unrecognized doubles in the catalogue but they are likely to be few and will not affect the statistics of the source counts.

#### 3.3.2 Positional Errors

The systematic error in the position of each sources was taken to be 0.1’’, which is a conservative estimate for the VLA under normal conditions and given good phase calibration, such as obtained for these observations (VLA Observational Status Summary, Taylor et al. 2002). The random positional error for an unresolved, or only slightly resolved, source is defined as the point-spread function (i.e.

the FWHM of the restoring beam,  $3.35''$ ) divided by twice the signal to noise ratio (see Condon 1997, for a thorough discussion). With a  $4\sigma$  source limit of  $30\ \mu\text{Jy}$  the maximum statistical error is  $0.42''$  giving a maximum total error of  $0.43''$ . We do not give positional errors for individual sources in our final catalogue (Table 1) but merely note here that the error varies between  $0.42''$  for the faintest sources, down to  $0.1''$  for the brightest non-extended sources. For the six extended sources mentioned in section 3.1 the positions of the optical counterparts are given which are accurate to  $0.3''$ .

### 3.3.3 The Catalogue

A sample of the catalogue of sources is presented in Appendix A in Table A1. The full Table containing 449 sources above a  $4\sigma$  peak flux density limit of  $30\ \mu\text{Jy}/\text{beam}$  appears in the electronic form of this paper.

## 4 THE SOURCE COUNTS

Our radio survey was designed primarily to investigate the relationship between the faint radio and faint X-ray source populations. However with an rms noise level of  $7.5\ \mu\text{Jy}/\text{beam}$  it reaches approximately the same depth as the deepest radio surveys yet made at 1.4 GHz, e.g.  $7.5\ \mu\text{Jy}/\text{beam}$  rms noise for the HDF, (Richards 2000);  $4.8$  and  $9.2\ \mu\text{Jy}/\text{beam}$  rms noise for the Lockman Hole East and the ELAIS N2 surveys, (Iverson et al. 2002);  $< 10\ \mu\text{Jy}$  for the Phoenix Deep Survey, Hopkins et al. 2003. Our survey is useful in its own right for studying the radio source counts at faint flux densities, where other surveys have shown an upturn, generally attributed to an additional contribution from starburst galaxies. In this section we derive the source counts from our present survey, compare them with those from other deep surveys and model the counts.

### 4.1 Completeness

In order to minimise the corrections for incompleteness, which become large at the lowest flux densities, we restrict our sample to sources which have a peak flux density  $> 5\sigma$ , i.e.  $37.5\ \mu\text{Jy}$  (before correcting for the primary beam attenuation).

Although we use a  $> 5\sigma$  peak detection threshold so that the number of false detections will be negligible, our source counts are based on total flux density. It is therefore possible that some very extended sources of low surface brightness may be missed. We, as Richards (2000), have searched for such sources using tapered maps, but have found very few. As the number of additional sources found when going from a  $3.3''$  to  $6''$  beam was very small, the number to be found when searching for even more extended sources is likely to also be very small, and so we do not consider them further.

In order to derive the source count density, we simply added up the number of sources in various total flux density bins of equal width in log space:  $\Delta S = 0.18 \log(\text{mJy})$ . The exception was the highest flux density bin where the upper limit was increased from  $682\ \mu\text{Jy}$  to  $1365\ \mu\text{Jy}$  to include all the remaining objects bar the 12 brightest where the flux density range greater than  $1365\ \text{mJy}$  is not well

**Table 1.** The 1.4 GHz Source Counts. The first column shows the bin range, the second one the bin centre (as explained in the text), the third column the number of sources found in that range, the fourth column shows the multiplicative correction for the biases described in the text and the final column shows the source counts per steradian, normalised to the Euclidean value, for each bin with Poisson errors derived from the number of sources in each bin.

Bin ( $\mu\text{Jy}$ )	$\langle S_{1.4} \rangle$ ( $\mu\text{Jy}$ )	$N_s$	Correction	$S^{2.5} \frac{dN}{dS}$ ( $\text{Jy}^{1.5} \text{sr}^{-1}$ )
37.50 - 56.76	46.75	94	2.67	$3.26 \pm 0.34$
56.76 - 85.91	70.76	126	1.23	$3.74 \pm 0.33$
85.91 - 130.03	107.10	92	1.00	$4.15 \pm 0.43$
130.03 - 196.80	162.11	48	1.00	$4.02 \pm 0.58$
196.80 - 297.87	245.36	25	1.00	$3.90 \pm 0.78$
297.87 - 450.85	371.37	16	1.00	$4.65 \pm 1.16$
450.85 - 1365.00	861.40	13	1.00	$5.18 \pm 1.44$

sampled. The centre of each bin was calculated using equation 19 of Windhorst et al. (1984) which is a function of the normalised differential source count slope (as directly measured from our data). Initially each bin centre was simply the mean of the flux density of the sources in each bin, but an iterative process was used to find the true bin centre by fitting the source count slope to our data after deriving new bin centres from this equation. After 3 iterations the slope stabilised at  $0.14 \pm 0.05$ , consistent with that found for the HDF over this region,  $0.12 \pm 0.13$  (Richards 2000) (although with a higher normalisation as discussed in section 4.2 and 4.3.4). The number of sources in each bin was corrected to take into account the number of sources missed by the source extraction algorithm, SAD, as explained in Section 3.2.1. The effective area, relative to the full  $30'$  X-ray survey area, was corrected to take into account the attenuation caused by the primary beam and by chromatic aberration, which increases radially away from the phase centre. The total correction for these effects for each bin is shown in Table 1 in which we also present our final source counts.

### 4.2 Comparison of our differential source counts with other results

A summary of recent determinations of the differential 1.4 GHz source counts is shown in Fig. 5 along with the results presented here. The counts are normalised to those counts expected from a non-expanding Euclidean universe (i.e.  $dN/dS \propto S^{-2.5}$ ). The keys to the various surveys are given on the figure itself.

The surveys presented in Fig 5 show a consistent upturn above a Euclidean normalised slope below  $1\ \text{mJy}$ . The upturn is interpreted as the presence of a second source population, in addition to the AGN population which is responsible for the sources at brighter flux densities. The second population is usually associated with relatively low radio luminosity galaxies at moderate redshifts ( $z \leq 1$ , e.g. Hopkins et al. 1998 and references therein) and the radio emission is thought to arise from starbursts (c.f. Benn et al. 1993; Helou et al. 1985).

Apart from the upturn, the most noticeable feature of the sub-mJy counts is the relatively wide variation between different surveys below  $1\ \text{mJy}$  where the upturn becomes no-

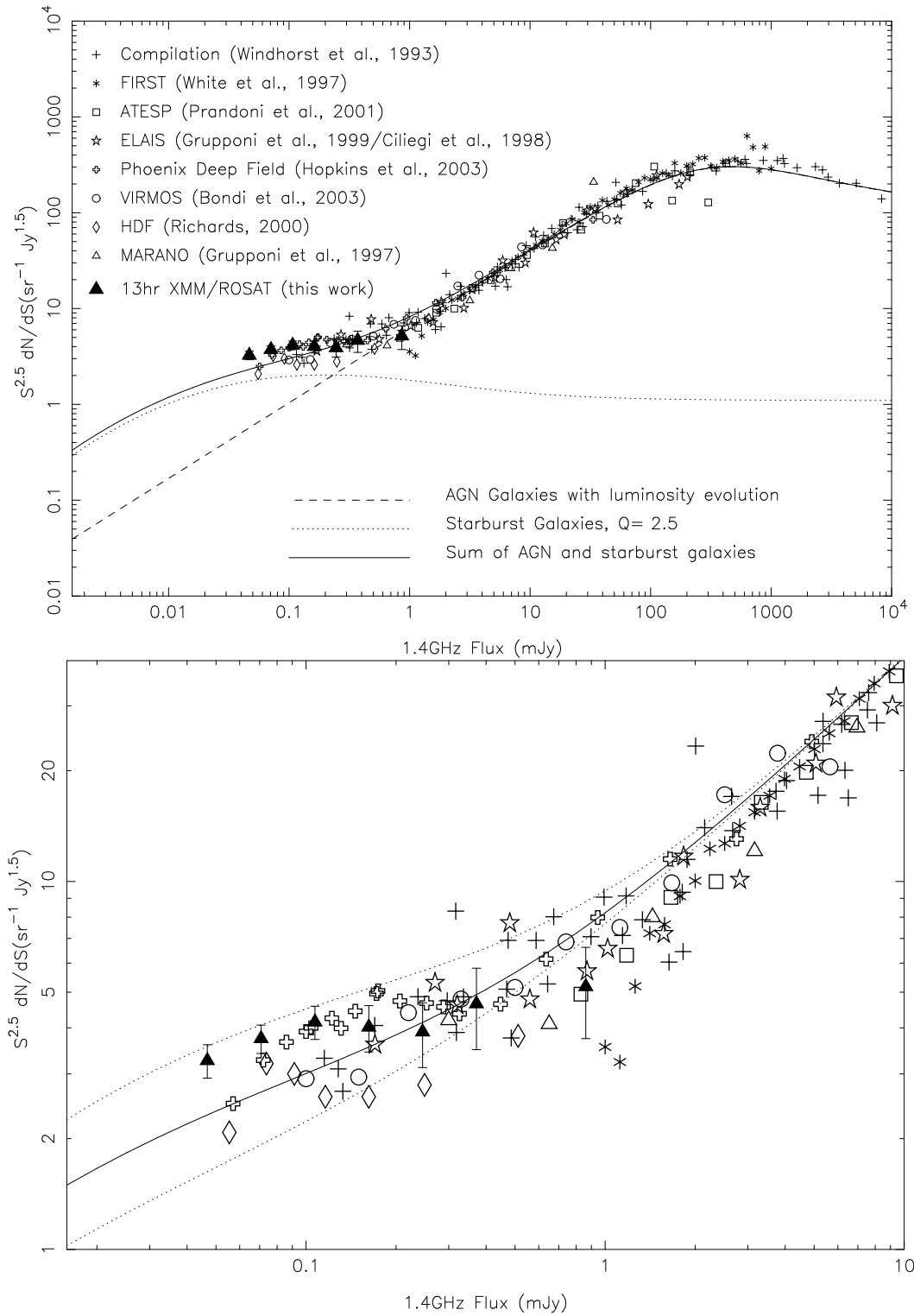


**Figure 5.** The 1.4GHz Differential Source Counts of this survey compared to other surveys, as indicated on the figure. **Top Panel** The solid line represents the combination of the modelled source counts due to AGN with luminosity evolution (dashed line) and the counts due to starforming galaxies (dotted line). **Bottom Panel** A close up of the sub-10 mJy region with the total model represented by a solid line with the evolutionary parameter,  $Q$ , for the starforming galaxies at 2.5. The dotted lines represent  $\pm 0.5$  variations on  $Q$ .

ticeable (see the close up in the lower panel of Fig. 5)<sup>2</sup>). The variation is greatest around 0.1 – 0.3 mJy where the HDF is significantly lower than the other surveys. The different surveys seem to re-converge below 0.1 mJy although one should caution that the various flux density correction factors are greatest at the faintest flux densities (Table 1. Most of the very deep surveys which sample the sub-mJy flux density range have similar, relatively small survey areas (30 – 40' diameter), where they are at their most sensitive, although the VIRMOS and full PDF surveys cover 1 and 4.5 square degrees respectively.

The difference between the Phoenix and HDF surveys has already been discussed by Richards (2000) and Hopkins et al. (2003). Georgakakis et al. (2000) note that the difference is larger than would be expected from the fluctuations associated with galaxy clustering. The differences therefore probably arise from differing selection criteria. As is clear from the presence of the bright radio source on the western edge of our field, our own survey area had no radio selection criteria! The only selection criterion was that galactic obscuration should be as low as we could find in the sky,  $N_H = 6.5 \times 10^{19} \text{ cm}^{-2}$ , confirmed by measurements of 100 $\mu\text{m}$  cirrus (McHardy et al. 1998). By contrast, the HDF survey was chosen to contain no radio sources > 1 mJy at 8.3 GHz (Williams et al. 1996). Minimising the number of bright sources in a field may also decrease the number of faint sources in the field as it is likely that bright and faint sources are similarly clustered to a reasonable extent<sup>3</sup>. As the HDF was also chosen to be free of bright sources at other wavelengths, particularly stars and bright nearby clusters of galaxies, and as sources which are bright at one wavelength are more likely to be bright at another, there are additional reasons why the HDF should be deficient in radio sources. The Phoenix Survey was also chosen to be free of bright radio sources, but with a much less stringent criteria than the HDF (> 100 mJy at 4.85 GHz). Our source counts (not selected to avoid bright sources) lie above the HDF counts and are consistent with the VIRMOS and PDF data from 0.2 – 1.0 mJy.

If the apparent differences between the HDF and other surveys at  $\sim 200\mu\text{Jy}$  are confirmed by deeper surveys still, then the two-component explanation of the source counts might account for the differences. For example, if the bump in the source counts is associated with emission from intermediate redshift ( $\sim 0.1 - 0.5$ ) starburst galaxies, but distant AGN again dominate at the very faintest flux densities, then the greater structure in the universe at intermediate redshifts might account for the variance in the source counts. The effect of large scale structure on faint source counts at these levels warrants further analysis, but detailed analysis is beyond the scope of this paper. However the possibility

of this effect is discussed briefly in the following section on modelling.

### 4.3 Modelling the source counts

Radio source counts have, from the earliest times, been used to examine the evolution over cosmological time of radio sources (Longair 1966; Rowan-Robinson 1970). It has been assumed that the evolution of the 1.4 GHz luminosity function at a given redshift,  $\phi_z$ , can be deconvolved into two components: luminosity and density evolution, parameterized thus (Condon 1984; Saunders et al. 1990; Rowan-Robinson et al. 1993; Hopkins et al. 1998):

$$\phi_z(L) = g(z)\phi_0\left(\frac{L}{f(z)}\right) \quad (2)$$

where  $g(z)$  and  $f(z)$  represent the density and luminosity evolution respectively and  $\phi_0$  is the luminosity function at  $z = 0$ .

The sub-mJy upturn in the normalised differential source counts is usually modelled assuming a contribution from starforming galaxies, for which there is increasing evidence (Benn et al. 1993; Gruppioni et al. 2003), in addition to that from the AGN (Condon 1984; Rowan-Robinson et al. 1993; Hopkins et al. 1998) which are associated with the most luminous radio sources (Dunlop & Peacock 1990). Rowan-Robinson et al. refer to the starforming galaxies (SFG) and AGN as spirals and ellipticals respectively, as the radio AGN are typically associated with early type galaxies and radio emission from spirals is normally associated with starformation. Here we fit the two-component model to our source counts.

To derive the flux density distribution of sources of any type, AGN or starburst, one can integrate the local luminosity function using a parameterisation of the evolution of sources and the chosen cosmology (throughout we use the cosmological parameters resulting from the WMAP observations (Bennett et al. 2003) i.e :  $\Omega_M = 0.27$ ,  $\Omega_\Lambda = 0.73$  and  $H_0 = 70 \text{ km s}^{-1} \text{ Mpc}^{-1}$ ).

$$dN(S) = \int \phi_z(L) d(\log_{10} L) dV \quad (3)$$

Density evolution is normally expressed as a function of redshift,  $g(z) \propto (1+z)^P$ . Therefore the number of objects within a certain flux density range can be expressed as a function of the flux density,  $S$ , and the redshift,  $z$ :

$$dN(S) = \int (1+z)^P \phi_0\left(\frac{L(S,z)}{f(z)}\right) \frac{dS}{S} dV_c(z) \quad (4)$$

where

$$L(S,z) = 4\pi SD_L^2(1+z)^{-\alpha-1}. \quad (5)$$

$D_L$  is the luminosity distance,  $\alpha$  is the spectral index of the radio source ( $S \propto \nu^\alpha$ ).  $dV_c(z)$  is the comoving volume element of solid angle  $d\Omega$  and redshift interval  $dz$  defined by Hogg (1999) thus:

$$dV_c(z) = D_H \frac{(1+z)^{-2} D_L^2}{(\Omega_M(1+z)^3 + \Omega_k(1+z)^2 + \Omega_\Lambda)^{\frac{1}{2}}} d\Omega dz \quad (6)$$

$$\text{i.e. } dV_c(z) = h(z)d\Omega dz \quad (7)$$

<sup>2</sup> The low values of the FIRST survey below 2 mJy are due to incompleteness as explained by White et al. (1997)

<sup>3</sup> Overzier et al. (2003) found that fainter sources were more weakly clustered than brighter sources in the NVSS and FIRST surveys (which are dominated by AGN) but below 5 mJy it was found that the clustering of AGN remains consistent (Wilman et al. 2003). The clustering of the radio faint starforming population remains unexplored, but may be more weakly clustered than AGNs below  $\sim 0.2 \text{ mJy}$  (Wilman et al. 2003).



where  $D_H$  is the Hubble distance ( $c/H_0$ ),  $\Omega_M$  matter density parameter,  $\Omega_\Lambda$  is the  $\Lambda$  density parameter and  $\Omega_k$  is the curvature term. Normalising to a non-expanding, Euclidean universe (i.e.  $dN/dS \propto S^{-2.5}$ ):

$$S^{2.5} \frac{dN}{dS} \propto S^{1.5} \int_0^\infty \phi_0(S, z) h(z) (1+z)^P dz \quad (8)$$

#### 4.3.1 AGN

The AGN luminosity function is taken from Dunlop & Peacock (1990), and shifted from 2.7 GHz to 1.4 GHz by Rowan-Robinson et al. (1993). Following Rowan-Robinson et al. (1993) we assume pure luminosity evolution and no density evolution. The sample consists of two components, a steep spectrum and a flat spectrum component.

Steep spectrum component:

$$\phi_0 \left( \frac{P_{1.4}}{P_c(z)} \right) = 10^{-6.91} \left[ \left( \frac{P_{1.4}}{P_c(z)} \right)^{0.69} + \left( \frac{P_{1.4}}{P_c(z)} \right)^{2.17} \right]^{-1} \quad (9)$$

where the luminosity evolution ( $P_c(z) = f(z)$ ) is described by

$$\log P_c(z) = 26.22 + 1.26z - 0.26z^2 \quad (10)$$

Flat spectrum component:

$$\phi_0 \left( \frac{P_{1.4}}{P_c(z)} \right) = 10^{-8.15} \left[ \left( \frac{P_{1.4}}{P_c(z)} \right)^{0.83} + \left( \frac{P_{1.4}}{P_c(z)} \right)^{1.96} \right]^{-1} \quad (11)$$

where

$$\log P_c(z) = 26.36 + 1.18z - 0.28z^2 \quad (12)$$

#### 4.3.2 Starburst Galaxies

The local SFG luminosity (with no evolution) is represented by the form proposed by Saunders et al. (1990).

$$\phi_0(L) = C \left( \frac{L}{L_*} \right)^{1-\alpha_f} \exp \left[ -\frac{1}{2\sigma^2} \log_{10}^2 \left( 1 + \frac{L}{L_*} \right) \right] \quad (13)$$

which has the advantage of behaving as a power law for  $L \ll L_*$  and as a Gaussian in  $\log L$  for  $L \gg L_*$ . Rowan-Robinson et al. use this form of the local luminosity density function derived from a complete sample of radio sources identified with optical spectra with a flux density above 0.1 mJy (Benn et al. 1993). Sadler et al. (2002) fit the same form to data obtained from the cross correlation of the 1.4 GHz NRAO VLA Sky Survey (NVSS) with the 2dF Galaxy Redshift Survey (2dFGRS). We used the latter fit as although the NVSS has a higher sensitivity limit than the survey of Benn et al. (1993) (2.3 mJy instead of 0.1 mJy), the Benn et al. sample is based on only 87 sources (56 identified as SFGs) whereas Sadler et al. (2002) have a final sample of 757 radio sources (242 identified as SFGs) and hence better represent the local luminosity distribution of starforming galaxies. The values given for this fit by Sadler et al. are  $\log_{10} C = -2.41 (\text{mag}^{-1} \text{Mpc}^{-3} h^3)$  ( $h = H_0/100$ ),  $\log_{10} L_* = 19.55$ ,  $\alpha_f = 0.840$  and  $\sigma = 0.940$  where the observed flux densities have been  $k$ -corrected assuming a mean spectral index of  $\alpha = -0.7$ .

#### 4.3.3 Total Source Counts

The total model source counts are the sum of the contributions from AGNs and SFGs. The AGN local luminosity function, as described in Section 4.3.1, is integrated up to a redshift of 5; integrating up to higher redshifts does not affect the contribution of AGNs as they would generally be too faint to be detected in surveys with limits of 0.01 – 0.1 mJy. We do not vary any of the parameters from those given in Section 4.3.1 and so the AGN contribution to the total source counts is fixed at the same level as that described by previous researchers.

The global space density of starformation rate of the universe increases sharply from the present epoch to  $z = 2$  (Madau et al. 1996, 1998; Lilly et al. 1996) and then is generally considered to be constant up to  $z = 5$  (Steidel et al. 1999; Haarsma et al. 2000; Thompson 2003), although there is some disagreement as to the exact form of the starformation history of the universe after  $z \sim 1.5$  (Lanzetta et al. 2002). We, as with Hopkins et al. (1998), therefore describe the luminosity evolution of the luminosity function of SFGs as  $(1+z)^Q$  from redshift 0 to 2, constant between redshifts 2 and 5. We do not consider starforming galaxies at higher redshifts where even the most luminous would be undetected at the detection limit of this survey. The only parameter which we allow to vary in our fit to the combined source counts is the parameter,  $Q$ . As with the AGN, there is no density evolution of the SFGs, ie  $P = 0$ . All other SFG parameters are fixed at the values derived by Sadler et al. (2002) and described in Section 4.3.2.

Due to the large variance between surveys, we have not performed a  $\chi^2$  fit to the source counts as the fit would depend greatly on which datasets were included. We have simply performed a fit-by-eye to find a solution which passes approximately through the middle of most of the data points. The value of  $Q$  which we thereby derive is 2.5 and the resultant fit is shown in Fig. 5. In that figure the SFG contribution is represented by a dotted line, the AGN contribution as a dashed line and the total source counts as a solid line. Our source counts are represented by solid triangles and several other surveys which reach below 1 mJy are also shown. In Fig. 5 we also illustrate the fits obtained with  $Q = 2.0$  and  $Q = 3.0$ , which lie towards the outer bounds of the distribution of source count points and so provide some estimate of the error on  $Q$ .

We note that our best estimate of  $Q$  deviates only very slightly from the values obtained by Hopkins et al. (1998) of  $Q = 3.1 \pm 0.8$ , Rowan-Robinson et al. (1993) of  $Q = 3.3 \pm 1.0$ , from the *IRAS* observations of Saunders et al. (1990) ( $Q = 3.2 \pm 0.1$ ), which are believed to be tracing the same starforming galaxies, and the value of Condon et al. (2002),  $Q = 3.0 \pm 1$ . Any differences probably result from the fact that we used the Sadler et al. luminosity function for starforming galaxies, our choice of a different cosmology to that of previous authors does significantly change the value of  $Q$ .

Although a two component AGN/SFG model may be over-simplistic as AGN and starforming activity often occur together in the same galaxy and are probably not entirely independent, nonetheless it does provide a reasonable explanation of the radio source counts at faint flux densities. The model is testable as the redshift distribution of each

population can be predicted and compared with observation when full optical spectroscopic follow-up has been completed. In addition, forthcoming *Spitzer* (Gallagher et al. 2003) observations of this field will distinguish SFGs and allow us to refine the the radio/IR correlation (Carilli & Yun 2000; Gruppioni et al. 2003).

#### 4.3.4 Variance Between Surveys

As we already noted, there is significant variance in the source density between surveys below 1mJy. The variations are of order  $\sim 50\%$  at flux density levels of a few hundred  $\mu\text{Jy}$ . If the major contributors at that flux density level are starburst galaxies, then we expect 1.4GHz radio luminosities of  $\sim 10^{22}$  to  $10^{24}$   $\text{W Hz}^{-1}$  (Gruppioni et al. 2003; Garrett 2002). A galaxy of luminosity  $\sim 10^{23}$   $\text{W Hz}^{-1}$ , with a flux density of  $200\mu\text{Jy}$ , would lie at a redshift of  $\sim 0.4$ . At this redshift, filamentary structure in the universe is already very well developed and may account for the variance between surveys. For example, at a redshift of 0.4, the angular size of our survey corresponds to  $\sim 9\text{Mpc}$ . The largest structures known locally (e.g. the Shapley supercluster) are around  $\sim 30\text{Mpc}$  (Quintana et al. 2000). To view this volume at a redshift  $z \sim 0.4$  an area of diameter  $\sim 2^\circ$  needs to be studied. There is also evidence of very large structures in the radio of  $\sim 100\text{Mpc}$  below redshift  $z \sim 0.4$  (Brand et al. 2003). To allow for structure on this scale would require surveys of diameter  $\sim 5^\circ$  at sensitivities below  $0.1\mu\text{Jy}$ , larger than even the largest survey of this depth, the *Spitzer* First Look Survey radio catalogue (e.g. Condon et al. 2003) which has a diameter of  $\sim 3^\circ$ .

Additionally, Bellanger & de Lapparent (1995 - see also Frith et al 2003) show that, at such a redshift, and locally, the Universe consists of filamentary structure (walls) separated by great voids. We may see evidence of one such wall in our own survey as a number of identifications of the *ROSAT* sources lie at a similar redshift of 0.38. The walls are of size  $\sim 100\text{Mpc}$  and voids have diameters of a few tens of Mpc. Our survey area is typical of other deep radio surveys and so, depending on whether the survey area happens to hit a large number of walls, or pass mainly through voids, large variations in source numbers may be expected. The Phoenix Deep Survey also appears to show the same kind of redshift clustering, suggestive of these features of large scale structure (Andrew Hopkins, private communication). No doubt our understanding of large scale radio structure at  $z \sim 0.4$  will improve with detailed analysis of the current surveys mentioned here and others.

## 5 CONCLUSIONS

From a total of  $\sim 25$  hours of data from the VLA at 1.4 GHz in both A and B configuration, 449 sources are detected down to a peak flux density  $4\sigma$  limit of  $30\mu\text{Jy}$  in a circular field of  $30'$  diameter. This survey is one of the most sensitive made at this frequency.

The source counts are similar to that of other deep surveys, showing an upturn of the Euclidean normalised source counts below 1 mJy and are similar to those of the deepest Phoenix sample (Hopkins et al. 2003), and both lie above

the counts from the HDF. The HDF may be underdense on account of its selection criteria.

As in other deep surveys we assume that the upturn of the source counts results from a starforming population at medium redshifts. We base our modelling of this population on the local galaxy luminosity function of Sadler et al. (2002), together with mild luminosity evolution. Although our source counts are similar to those of Hopkins et al. (2003), our modelling results in a slightly different value of the luminosity evolution parameter,  $Q$ , probably due to our choice of the Sadler et al. local luminosity function (the choice of a different cosmology to that of previous authors does not strongly affect this value). Future guaranteed *Spitzer* observations of this field will help distinguish the SFG and AGN contributions and refine the two component model of the source counts.

## ACKNOWLEDGMENTS

We would like to thank the referee, Andrew Hopkins, for very constructive comments particularly with the modelling. Also we thank the staff of the VLA for providing the data described here, and Tom Muxlow for help in calibrating the data. NS acknowledges receipt of a PPARC studentship and support by the *Probing the Origin of the Extragalactic background (POE)*, European Network number HPRN-CT-2000-00138. IMcH acknowledges the support of a PPARC Senior Research Fellowship, and KFG was supported by PPARC grant PPA/G/S/1999/00102.

## REFERENCES

- Bellanger C., de Lapparent V., 1995, ApJL, 455, L103+
- Benn C. R., Rowan-Robinson M., McMahon R. G., Broadhurst T. J., Lawrence A., 1993, MNRAS, 263, 98
- Bennett C. L., Halpern M., Hinshaw G., Jarosik N., Kogut A., Limon M., Meyer S. S., Page L., Spergel D. N., 2003, ApJS, 148, 1
- Bondi M., Ciliegi P., Zamorani G., Gregorini L., Vettolani G., Parma P., de Ruiter H., Le Fevre O., Arnaboldi M., Guzzo L., 2003, A&A, 403, 857
- Brand K., Rawlings S., Hill G. J., Lacy M., Mitchell E., Tufts J., 2003, MNRAS, 344, 283
- Carilli C. L., Yun M. S., 2000, ApJ, 530, 618
- Ciliegi P., McMahon R. G., Miley G., Gruppioni C., Rowan-Robinson M., Cesarsky C., Danese L., Franceschini A., Genzel R., Lawrence A., Lemke D., Oliver S., Puget J.-L., Rocca-Volmerange B., 1999, MNRAS, 302, 222
- Condon J. J., 1984, ApJ, 284, 44
- Condon J. J., 1989, ApJ, 338, 13
- Condon J. J., 1992, ARA&A, 30, 575
- Condon J. J., 1997, PASP, 109, 166
- Condon J. J., Cotton W. D., Broderick J. J., 2002, AJ, 124, 675
- Condon J. J., Cotton W. D., Yin Q. F., Shupe D. L., Storrie-Lombardi L. J., Helou G., Soifer B. T., Werner M. W., 2003, AJ, 125, 2411
- Dunlop J. S., Peacock J. A., 1990, MNRAS, 247, 19

- Frith W. J., Buswell G. S., Fong R., Metcalfe N., Shanks T., 2003, *MNRAS*, 345, 1049
- Gallagher D. B., Irace W. R., Werner M. W., 2003, in *IR Space Telescopes and Instruments*. Edited by John C. Mather . *Proceedings of the SPIE*, Volume 4850, pp. 17-29 (2003). Development of the Space Infrared Telescope Facility (SIRTF). pp 17-29
- Garrett M. A., 2002, *A&A*, 384, L19
- Garrett M. A., Muxlow T. W. B., Garrington S. T., Alef W., Alberdi A., van Langevelde H. J., Venturi T., Polatidis A. G., Kellermann K. I., Baan W. A., Kus A., Wilkinson P. N., Richards A. M. S., 2001, *A&A*, 366, L5
- Georgakakis A., Mobasher B., Cram L., Hopkins A., Rowan-Robinson M., 2000, *A&AS*, 141, 89
- Gruppioni C., Ciliegi P., Rowan-Robinson M., Cram L., Hopkins A., Cesarsky C., Danese L., Franceschini A., Genzel R., Lawrence A., Lemke D., McMahon R. G., Miley G., Oliver S., Puget J.-L., Rocca-Volmerange B., 1999, *MNRAS*, 305, 297
- Gruppioni C., Pozzi F., Zamorani G., Ciliegi P., Lari C., Calabrese E., Franca F. L., Matute I., 2003, *MNRAS*, 341, L1
- Gunn K. F., M<sup>c</sup>Hardy I. M., Almaini O., Shanks T., Sumner T. J., Muxlow T. W. B., Efstathiou A., Jones L. R., Croom S. M., Manners J. C., Newsam A. M., Mason K. O., Serjeant S. B. G., Rowan-Robinson M., 2001, *MNRAS*, 324, 305
- Gunn K. F., M<sup>c</sup>Hardy I. M., Seymour N., Newsam A. M., Page M. J., Mason K. O., Loaring N. S., Jones L. R., Muxlow T., Takata T., Sekiguchi K., Sasseen T., 2003, *Astronomische Nachrichten*, 324, 105
- Haarsma D. B., Partridge R. B., Windhorst R. A., Richards E. A., 2000, *ApJ*, 544, 641
- Halpern J. P., Helfand D. J., Moran E. C., 1995, *ApJ*, 453, 611
- Helou G., Soifer B. T., Rowan-Robinson M., 1985, *ApJL*, 298, L7
- Hogg D. W., 1999, *astro-ph/9905116*
- Hopkins A. M., Afonso J., Chan B., Cram L. E., Georgakakis A., Mobasher B., 2003, *AJ*, 125, 465
- Hopkins A. M., Mobasher B., Cram L., Rowan-Robinson M., 1998, *MNRAS*, 296, 839
- Iverson R. J., Greve T. R., Smail I., Dunlop J. S., Roche N. D., Scott S. E., Page M. J., Stevens J. A., Almaini O., Blain A. W., Willott C. J., Fox M. J., Gilbank D. G., Serjeant S., Hughes D. H., 2002, *MNRAS*, 337, 1
- Lanzetta K. M., Yahata N., Pascarella S., Chen H., Fernández-Soto A., 2002, *ApJ*, 570, 492
- Lilly S. J., Le Fevre O., Hammer F., Crampton D., 1996, *ApJL*, 460, L1+
- Longair M. S., 1966, *MNRAS*, 133, 421
- Madau P., Ferguson H. C., Dickinson M. E., Giavalisco M., Steidel C. C., Fruchter A., 1996, *MNRAS*, 283, 1388
- Madau P., Pozzetti L., Dickinson M., 1998, *ApJ*, 498, 106
- Moran E. C., Lehnert M. D., Helfand D. J., 1999, *ApJ*, 526, 649
- M<sup>c</sup>Hardy I. M., Jones L. R., Merrifield M. R., Mason K. O., Newsam A. M., Abraham R. G., Dalton G. B., Carrera F., Smith P. J., Rowan-Robinson M., Abraham R. G., 1998, *MNRAS*, 295, 641
- M<sup>c</sup>Hardy I. M., Gunn K. F., Newsam A. M., Mason K. O., Page M. J., Takata T., Sekiguchi K., Sasseen T., Cordova F., Jones L. R., Loaring N., 2003, *MNRAS*, 342, 802
- Overzier R. A., Röttgering H. J. A., Rengelink R. B., Wilman R. J., 2003, *A&A*, 405, 53
- Prandoni I., Gregorini L., Parma P., de Ruiter H. R., Vettolani G., Wieringa M. H., Ekers R. D., 2000, *A&AS*, 146, 41
- Prandoni I., Gregorini L., Parma P., de Ruiter H. R., Vettolani G., Wieringa M. H., Ekers R. D., 2001, *A&A*, 365, 392
- Quintana H., Carrasco E. R., Reisenegger A., 2000, *AJ*, 120, 511
- Richards E. A., 2000, *ApJ*, 533, 611
- Rowan-Robinson M., 1970, *MNRAS*, 149, 365
- Rowan-Robinson M., Benn C. R., Lawrence A., McMahon R. G., Broadhurst T. J., 1993, *MNRAS*, 263, 123
- Sadler E. M., Jackson C. A., Cannon R. D., McIntyre V. J., Murphy T., Bland-Hawthorn J., Bridges T., Cole S., Colless M., 2002, *MNRAS*, 329, 227
- Saunders W., Rowan-Robinson M., Lawrence A., Efstathiou G., Kaiser N., Ellis R. S., Frenk C. S., 1990, *MNRAS*, 242, 318
- Seymour N., 2002, PhD thesis, School of Physics and Astronomy, University of Southampton, <http://www2.iap.fr/users/seymour/>
- Smail I., Owen F. N., Morrison G. E., Keel W. C. and Ivison R. J., J. L. M., 2002, *ApJL*, *astro-ph/0208434*
- Steidel C. C., Adelberger K. L., Giavalisco M., Dickinson M., Pettini M., 1999, *ApJ*, 519, 1
- Taylor G. B., Carilli C. L., A. P. R., eds, 1999, *Synthesis Imaging in Radio Astronomy II*. NRAO
- Taylor G. B., Ulvestad J. S., Perley R. A., 2002, *The Very Large Array Observational Status Summary*
- Thompson R. I., 2003, *ApJ* in press, *astro-ph/0306594*
- White R. L., Becker R. H., Helfand D. J., Gregg M. D., 1997, *ApJ*, 475, 479
- Williams R. E., Blacker B., Dickinson M., Dixon W. V. D., Ferguson H. C., Fruchter A. S., Giavalisco M., Gilliland R. L., Heyer I., Katsanis R., Levay Z., Lucas R. A., McElroy D. B., Petro L., Postman M., Adorf H., Hook R., 1996, *AJ*, 112, 1335
- Wilman R. J., Röttgering H. J. A., Overzier R. A., Jarvis M. J., 2003, *MNRAS*, 339, 695
- Windhorst R., Mathis D., Neuschaefer L., 1990, in *ASP Conf. Ser. 10: Evolution of the Universe of Galaxies The evolution of weak radio galaxies at radio and optical wavelengths*. pp 389-403
- Windhorst R. A., van Heerde G. M., Katgert P., 1984, *A&AS*, 58, 1

## APPENDIX A: THE 1.4 GHz SOURCE CATALOGUE

Here we present a sample of the complete 1.4 GHz source catalogue. The full catalogue appears in the electronic online version of this paper. Sources are ordered by total flux density and the first column gives a source's position in the catalogue. Columns 2,3 and 4 are the Right Ascension (hrs min secs) and columns 5,6 and 7 are the Declination (degrees mins secs). Column 8 is the mean angular size of a source (zero means it is unresolved). Column 9 is the signal

to noise ratio before corrections are made for the attenuation of the primary beam. Columns 10, 11 and 12 are the peak flux density, integrated flux density and the error of the total flux density all corrected for the primary beam attenuation and bandwidth smearing.

This paper has been typeset from a  $\text{\TeX}$ / $\text{\LaTeX}$  file prepared by the author.

**Table A1.** Complete 1.4 GHz Source Catalogue (source number, RA, dec, mean angular size, SNR, peak flux density, integrated flux density and error).

Source	Right Ascension hh mm ss	Declination °''	$\theta_{dec}$ ('')	$\sigma_{snr}$	$S_{peak}$ ( $\mu\text{Jy}$ )	$S_{integrated}$ ( $\mu\text{Jy}$ )	$\Delta S$ ( $\mu\text{Jy}$ )
1	13 33 29.040	37 55 57.90	35.0	1117.9	13985.2	92681.0	256.5
2	13 33 21.353	37 54 15.75	70.0	53.0	400.0	12554.7	598.5
3	13 34 3.011	37 59 49.18	1.8	1160.7	10539.6	11624.0	20.6
4	13 34 38.496	38 06 27.01	2.1	999.9	10980.8	10939.0	23.4
5	13 35 16.664	38 00 8.19	3.5	515.7	4946.5	8017.0	26.9
6	13 33 59.951	37 49 11.64	12.5	236.3	2227.9	3918.8	498.8
7	13 34 57.650	37 50 29.40	25.5	79.4	653.0	3680.7	150.2
8	13 34 38.015	37 57 10.33	13.5	109.3	833.1	2510.5	178.6
9	13 35 6.603	38 03 48.64	2.0	210.7	2176.6	2260.0	22.0
10	13 34 49.260	38 05 52.50	27.5	51.7	555.8	2146.9	108.4
11	13 35 25.340	38 05 33.90	23.0	42.0	569.8	1790.6	125.5
12	13 34 38.106	37 41 33.46	2.3	150.1	1836.5	1715.0	26.1
13	13 35 35.475	37 53 14.30	2.1	124.5	1359.6	1362.4	21.8
14	13 34 13.571	37 45 39.30	4.3	56.0	557.8	1112.0	33.8
15	13 34 5.407	38 07 37.99	3.5	70.9	955.0	1103.2	38.0
16	13 33 46.583	38 00 22.26	2.4	90.5	974.2	1041.9	27.1